



# Modeling the seasonal variability of phytoplankton in the subarctic northeast Pacific Ocean

Hao-Ran Zhang<sup>1</sup>, Yuntao Wang<sup>1,\*</sup>, Peng Xiu<sup>2</sup>, Fei Chai<sup>1,3</sup>

<sup>1</sup>State Key Laboratory of Satellite Ocean Environment Dynamics, Second Institute of Oceanography, Ministry of Natural Resources, Hangzhou 300012, PR China

<sup>2</sup>State Key Laboratory of Tropical Oceanography, South China Sea Institute of Oceanology, Chinese Academy of Sciences, Guangzhou 510301, PR China

<sup>3</sup>School of Marine Sciences, University of Maine, Orono, ME 04469, USA

**ABSTRACT:** The subarctic northeast Pacific Ocean (SNEP) is a high-nitrate, low-chlorophyll region where, due to iron (Fe) limitation, chlorophyll *a* (chl *a*) concentration is persistently low throughout the year despite abundant nitrate. Observations from a Biogeochemical-Argo float (BGC-Argo) deployed in the SNEP in 2012 show prominent variations in chl *a* in the upper ocean (0–150 m). Chl *a* peaks in late summer and autumn at a value >3 times that in winter; these observations at a fine resolution can help us disentangle the mechanisms driving the full seasonal cycle of phytoplankton. A one-dimensional physical–biogeochemical coupled model was applied at OSP to investigate the factors driving phytoplankton dynamics in the SNEP. Seasonal variability of chl *a* in the upper layer is reproduced by the model; results are reasonably comparable to the BGC-Argo observations in 2012 near OSP. Phytoplankton growth is limited in winter by the deep mixed layer, which reduces light availability; light gradually increases later in the year due to shoaling of the mixed layer and increasing solar radiation. In spring and early summer, Fe limitation restricts phytoplankton growth, especially diatoms, and grazing pressure on small phytoplankton from overwintering microzooplankton inhibits accumulation of phytoplankton biomass. Chl *a* accumulates throughout the summer, peaking in late summer and autumn as mesozooplankton consume microzooplankton, which reduces microzooplankton grazing on phytoplankton. Although the model study was restricted to the seasonal pattern of BGC-Argo observations in 2012, it nevertheless fully describes seasonal variability in chl *a* in the SNEP and is crucial to understanding mechanisms underlying phytoplankton dynamics in high-nitrate, low-chlorophyll regions.

**KEY WORDS:** Iron limitation · High-nitrate low-chlorophyll · Microzooplankton grazing · Physical–biogeochemical coupled model · Phytoplankton dynamics · Seasonal variability

## 1. INTRODUCTION

Phytoplankton are the main primary producers in marine ecosystems; they generate more than 45% of global photosynthetic net primary production with only 1% of the global photosynthetic biomass (Simon et al. 2009). For the majority of the global ocean, phytoplankton biomass is influenced by biological–chemical and physical processes (Mann & Lazier 1996). In particular, the photosynthesis rate of phyto-

plankton is controlled by temperature, nutrient uptake, and light availability, while phytoplankton loss is closely related to natural mortality representing remineralization and zooplankton grazing (Sigman & Hain 2012). Phytoplankton growth is affected by the availability of light and nutrients, which is affected by local dynamics, e.g. vertical mixing. During winter, mixing transports nutrients into the euphotic zone in oligotrophic regions (Behrenfeld 2010) and transports phytoplankton out of the euphotic zone

\*Corresponding author: yuntao.wang@sio.org.cn

(Sverdrup 1953). Additionally, vertical mixing can dilute or aggregate phytoplankton and zooplankton in the surface layer, which can influence phytoplankton biomass directly by changing the grazing rate of zooplankton (Behrenfeld & Boss 2014). Variations in multiple factors drive the complex response of phytoplankton biomass, and investigating phytoplankton dynamics is an important part of understanding changes in global ecosystems and the carbon cycle. This is particularly true for high-latitude oceans, e.g. the subarctic Pacific Ocean, where marine primary production is prominent (Huston & Wolverton 2009).

High-latitude seas usually exhibit strong seasonality in meteorological and water column properties, e.g. the incident light and mixed layer depth (MLD; Kara et al. 2003, Sasai et al. 2016). These physical forcings drive seasonal variability in phytoplankton biomass, which is usually gauged using chlorophyll *a* (chl *a*) concentration (Mochizuki et al. 2002). The onset of large increases in chl *a*, namely, phytoplankton blooms, is commonly observed during spring and early summer (Obayashi et al. 2001, Henson et al. 2009). However, the subarctic northeast Pacific Ocean (SNEP) exhibits a predominant difference in the seasonal variability of chl *a*. Chl *a* in the SNEP shows relatively little variation within the year, with a slight increase in late summer (Evans & Parslow 1985). However, the corresponding peak does not reach the magnitude of the phytoplankton bloom seen in other high-latitude portions of the North Pacific, where phytoplankton blooms occur in spring and early summer (Parsons & Lalli 1988). The mechanism of this unique seasonal variability of phytoplankton has been actively investigated by a series of biogeochemical studies, including observations and numerical models (Denman & Peña 1999, Harrison et al. 1999, Westberry et al. 2016).

Ocean Station Papa (OSP; 50° N, 145° W) in the SNEP has one of the longest time series of observations (Freeland 2007). The region near OSP is characterized as a low-advection system where the coastal influence is less prominent and long-term observations are suitable for investigating the influence of regional processes on phytoplankton variability (Bif & Hansell 2019). The SNEP is characterized as a high-nitrate, low-chlorophyll (HNLC) region where the surface nitrate (NO<sub>3</sub>) concentration is persistently sufficiently abundant for the growth of phytoplankton, though its value decreases from winter to summer as it is consumed by phytoplankton (Harrison 2002). Two hypotheses have been proposed to explain the weak increase in chl *a* during summer despite sufficient NO<sub>3</sub> levels: iron (Fe) limitation and

zooplankton grazing control (Banse 1991, Martin et al. 1991, Landry et al. 1993, Boyd et al. 2004). Specifically, shipboard Fe-enrichment experiments have shown that the addition of dissolved Fe to *in situ* water resulted in the utilization of most of the excess NO<sub>3</sub> and an increase in chl *a* (Martin & Fitzwater 1988, Martin et al. 1989, Marchetti et al. 2006). Thus, the scarcity of bioavailable Fe (BFe) at OSP limits the growth of marine phytoplankton.

Chl *a* in the SNEP is dominated by small phytoplankton (Yang et al. 2018), which are top-down controlled by the grazing of zooplankton, in particular by microzooplankton (Miller et al. 1991). *In situ* measurements have suggested that the grazing rates of large grazers, e.g. mesozooplankton, are too low to graze down the phytoplankton production in the subarctic Pacific Ocean (Dagg 1993, Harrison et al. 2004). Microzooplankton biomass in the SNEP remains relatively stable throughout the year (Boyd et al. 1995, Strom et al. 2000). In winter, the mixing, though it reaches its greatest depth in the year, is shallower than that in other regions at the same latitude, where both phytoplankton and microzooplankton are maintained at low levels and the growth of phytoplankton is balanced by microzooplankton grazing (Boyd & Harrison 1999, Peña & Varela 2007). Microzooplankton overwintering introduces continuous grazing pressure on the small phytoplankton biomass after winter, resulting in a less prominent spring bloom of phytoplankton at OSP (Frost 1993, Harrison et al. 2004). The increased microzooplankton grazing pressure on small phytoplankton weakens in summer because of the rapid growth of mesozooplankton, which graze on microzooplankton and consequently facilitate phytoplankton growth (Landry et al. 1993, Harrison et al. 1999). Thus, phytoplankton biomass is simultaneously modulated by nutrient supply and zooplankton grazing pressure (Banse 1991, Landry et al. 1997).

Additionally, other parameters, e.g. physical and biological factors, have been observed to play a role in the seasonal variability of phytoplankton biomass. For example, solar radiation determines the rate of photosynthesis, and low irradiance in winter has been shown to limit phytoplankton growth (Maldonado et al. 1999). However, the relationship between light availability and primary production over the entire year and its importance relative to that of other factors at OSP is unclear (Peña & Varela 2007).

Along with observations, marine ecosystem models have been used to probe hypotheses and gain further insights into ecosystem dynamics in the SNEP. Earlier modeling studies at OSP utilized a one-dimensional

(1D) ecosystem model to investigate factors determining phytoplankton biomass (Evans & Parslow 1985, Frost 1987, 1993). Their results confirmed the importance of microzooplankton grazing in controlling phytoplankton biomass throughout the year. As the Fe hypotheses have become widely adopted (Boyd et al. 1998), the Fe cycle and its role in regulating phytoplankton growth have been incorporated into ecosystem models (Denman & Peña 1999, 2002). These models are helpful in evaluating the role of Fe in modulating phytoplankton growth in concert with microzooplankton grazing. In particular, Fe limitation reduces the maximum specific growth rate (SGR) of phytoplankton, and models can reproduce the low phytoplankton biomass and weak seasonal cycle of surface  $\text{NO}_3$  concentrations in the HNLC region (Denman & Peña 1999). Subsequent models have been used to conduct sensitivity experiments to explore the impact of Fe limitation on phytoplankton growth and have found that phytoplankton biomass dramatically increases as Fe becomes sufficient (Peña 2003). However, there are still some deficiencies in reproducing observations with ecosystem models: the simulated surface phytoplankton biomass and chl *a* peak in spring in the model, but the observed maximum occurs in late summer (Peña & Varela 2007). This discrepancy can be attributed to previous studies focusing on reproducing the persistently low phytoplankton biomass in the SNEP, while the roles of different factors in influencing phytoplankton growth in each season have not been fully explored.

Recently, new observations, such as those from a Biogeochemical-Argo float (BGC-Argo), have been performed at OSP at high frequencies, i.e. at approximately 5 d intervals (Plant et al. 2016). Compared with cruise observations, which occur 2 or 3 times  $\text{yr}^{-1}$ , the BGC-Argo observational profiles capture the full seasonal cycles of biogeochemical factors. Indeed, BGC-Argo observations have shown that the surface chl *a* (SCHL) remains at a high value, 3 times higher than that in winter, from July to October (Schallenberg et al. 2017). The difference between phytoplankton biomass in winter and late summer is much larger than that in traditional records, suggesting that the late summer-to-autumn maximum is an important characteristic of phytoplankton seasonal variability at OSP (Westberry et al. 2016). However, the underlying mechanisms determining the seasonal cycles of phytoplankton at OSP have rarely been investigated in previous studies. By incorporating observational data from BGC-Argo, a new perspective for understanding phytoplankton dynamics is expected to be developed.

In this study, a 1D physical–biological model equipped with an Fe cycle was applied to investigate the phytoplankton dynamics and corresponding seasonal variability at OSP. To evaluate the model's performance in reproducing the physical and biogeochemical processes at OSP, the simulated results were validated with observational data from BGC-Argo and other platforms. The model results were used to analyze the driving mechanism of the seasonal variability in phytoplankton biomass. The factors controlling the seasonal variability of phytoplankton were comprehensively investigated, together with the importance of the different factors in determining the phytoplankton biomass in each season.

## 2. MODEL AND DATA

### 2.1. 1D coupled model

A 1D physical–biogeochemical (Ma et al. 2019) coupled model incorporating the Fe cycle (Xiu & Chai 2021) was applied at OSP. The physical model was based on the Regional Ocean Modeling System (ROMS); lateral processes were ignored. Previous studies have suggested that vertical mixing has a stronger effect on phytoplankton dynamics than advections in this region (Kawamiya et al. 1995, Denman & Peña 1999, Bif & Hansell 2019). There are 300 layers in the vertical direction that extend to 4000 m in depth, with a finer resolution near the surface.

The biogeochemical model used in this study was based on a newly developed carbon silicate nitrate ecosystem-Fe (CoSiNE-Fe) model (Xiu & Chai 2021). It has 2 phytoplankton groups (picoplankton [ $S_1$ ,  $\text{CHL}_1$ ,  $S_{1\text{Fe}}$ ] and diatoms [ $S_2$ ,  $\text{CHL}_2$ ,  $S_{2\text{Fe}}$ ]), 2 zooplankton groups (microzooplankton [ $zz_1$ ,  $zz_{1\text{Fe}}$ ] and mesozooplankton [ $zz_2$ ,  $zz_{2\text{Fe}}$ ]), 2 size classes of particulate organic nitrogen (small [ $S_{\text{PON}}$ ,  $S_{\text{PFe}}$ ] and large [ $L_{\text{PON}}$ ,  $L_{\text{PFe}}$ ]), 2 size classes of biogenic silica (small [ $S_{\text{bSi}}$ ] and large [ $L_{\text{bSi}}$ ]), 4 inorganic nutrients ( $\text{NO}_3$ , ammonium [ $\text{NH}_4$ ], phosphate [ $\text{PO}_4$ ], and silicate [ $\text{SiOH}_4$ ]), dissolved oxygen (DO), carbonate variables (dissolved inorganic carbon [DIC] and total alkalinity [ $T_{\text{ALK}}$ ]), 3 size classes of dust particles (dust particles [ $\text{Part}_{\text{Dust}}$ ,  $\text{Dust}_{\text{Fe}}$ ], large lithogenic particles [ $\text{Lith}_{\text{PartL}}$ ,  $\text{Lith}_{\text{LFe}}$ ], and small lithogenic particles [ $\text{Lith}_{\text{PartS}}$ ,  $\text{Lith}_{\text{SFe}}$ ]), truly soluble Fe ( $\text{Fe}_{\text{Sol}}$ ), colloidal Fe ( $\text{Fe}_{\text{Col}}$ ), strong and weak Fe ligands ( $\text{Fe}_{\text{LgS}}$ ,  $\text{Fe}_{\text{LgW}}$ ), and strong and weak ligands ( $\text{LgS}$ ,  $\text{LgW}$ ).

The Fe in particles can be transformed into  $\text{Fe}_{\text{Col}}$  and  $\text{Fe}_{\text{Sol}}$  by redissolution and photoreduction, respectively.  $\text{Fe}_{\text{Col}}$  is formed from  $\text{Fe}_{\text{Sol}}$  and is removed from the dissolved pool through colloidal aggregation.

In this study, BFe includes both soluble and ligand Fe, whereas  $Fe_{Col}$  is assumed not to be directly accessible by phytoplankton (Jiang et al. 2013). The growth of small phytoplankton and diatoms depends on light, temperature, and nutrients. The losses of phytoplankton in biological processes occur due to remineralization, which represents mortality, aggregation, and zooplankton grazing. The mortality of phytoplankton and zooplankton and the aggregation of small phytoplankton and diatoms form detritus, which is remineralized into inorganic matter during sinking (Ma et al. 2019). In terms of grazing, microzooplankton graze on small phytoplankton, while mesozooplankton graze on diatoms, microzooplankton, and both small and large particulate organic nitrogen. The overwintering of microzooplankton was modeled following Fujii et al. (2007) by adding a threshold of the minimum value of microzooplankton required for mesozooplankton to graze. In the model, chl *a* was simulated according to the photoacclimation assumption, with the variable chl *a*-to-phytoplankton biomass ratio (Fennel & Boss 2003) following Ma et al. (2019). Model equations and parameters are presented in the Supplement (see Text S1, Tables S1 & S2 at [www.int-res.com/articles/suppl/m680p033\\_supp.pdf](http://www.int-res.com/articles/suppl/m680p033_supp.pdf)).

The National Centers for Environmental Prediction (NCEP) reanalysis data from 2012 at OSP were extracted to produce the 6-hourly forcings (Kalnay et al. 1996). The parameterizations of the selected air-sea fluxes were adopted from Ma et al. (2019). In addition, the forcing data file included atmospheric deposition data ( $Fe_{Sol}$  deposition and lithogenic particle deposition) from Chien et al. (2016), with both dust and nondust sources (Fig. S1). Due to the lack of real-time data, climatological seasonal deposition fluxes were used in the model, which did not include dust from other episodic events. The 1 yr observations of temperature and salinity from BGC-Argo (float ID: 7601StnP) were averaged at monthly intervals. The initial model conditions for temperature, salinity,  $NO_3$ , and oxygen were obtained from the January BGC-Argo measurements;  $PO_4$  and  $SiOH_4$  were obtained from the World Ocean Atlas 2018 (WOA18) in January (Garcia et al. 2018). The 1D model ran for 10 yr using the forcing data of 2012 to reach a quasi-steady state; the analysis was conducted by averaging the last 5 yr of model output.

The MLD was calculated as the depth at which the density was equal to the density at 10 m plus  $0.03 \text{ kg m}^{-3}$  (de Boyer Montegut et al. 2004). The upper water column total chl *a*, phytoplankton biomass, zooplankton biomass, phytoplankton growth (representing phytoplankton primary production), phytoplank-

ton remineralization, zooplankton grazing, zooplankton excretion, and phytoplankton aggregation were integrated from the surface to 200 m. At OSP, the vertical structure of the chlorophyll concentration varies throughout the year; e.g. in winter it is evenly distributed within 100 m but concentrated within 30 m in summer. By integrating to a depth that is much deeper than the mixed layer, the effect of the mixed layer and vertical distribution of biomass has little influence on the depth-integrated values, although the variation in the water column is incorporated. The averaged regulating factors (nutrients, temperature, and light), limiting nutrients (nitrogenous nutrients,  $PO_4$ , and BFe), SGR, specific mortality rate, specific aggregation rate, and specific grazing rate of small phytoplankton were calculated by vertically integrating their values, which were weighted and normalized to the corresponding small phytoplankton biomass. The equation is defined as follows:

$$\overline{rate} = \frac{\sum_i^n rate(i) \times S1(i)}{\sum_i^n S1(i)} \quad (1)$$

where  $\overline{rate}$  is the rate averaged within the water column, *rate* is the rate of biological activity of small phytoplankton, *S1* is the small phytoplankton biomass, *i* is the layer of the model, and *n* is the total number of layers of the model. This method of vertical integration has been applied to investigate factors controlling phytoplankton growth in previous modeling studies (Fujii et al. 2005, 2007).

## 2.2. Cruise-based Fe, float, and satellite data

The observed dissolved Fe data in February 2013 are from the GEOTRACES Historical TEI Data (Tagliabue et al. 2012), and the data in August 2013 are obtained from Schallenberg et al. (2015). The former archived a global database of dissolved Fe observations with filter sizes ranging from 0.2 to  $0.45 \mu\text{m}$ , while the latter measured the Fe fraction that passes through a  $0.2 \mu\text{m}$  filter.

A biogeochemical profiling float (7601StnP; Teledyne/Webb Research Autonomous Profiling Explorer APEX) was assembled at the University of Washington and deployed at OSP starting in February 2012 (Plant et al. 2016). To evaluate model performance, the result was compared with the BGC-Argo observations for a whole year, i.e. from February 2012 to January 2013. Since 2014, the BGC-Argo float moved to a range that is more than 300 km from OSP, and the associated bottom depth varies between 2000 and 4000 m (Fig. S2), which cannot be simulated with

the 1D model. In addition to temperature and salinity sensors, the float was equipped with an *in situ* ultraviolet spectrophotometer (ISUS) optical nitrate sensor, Aandera model 3830 optical oxygen sensor, and WetLabs FLBB optical chlorophyll fluorescence and backscatter sensors (Haskell et al. 2020). The resolution of the 60 sampling depths increases as the floats ascended from their 1000 m parking depth to the shallowest sampling depth of 7 m in order to capture the higher variability in the surface waters. Specifically, variables were measured at 50 m intervals below 400 m, at 10 m intervals between 400 and 100 m, and at 5 m intervals above 100 m. Quality control of the float data had already been performed in previous studies (Plant et al. 2016, Schallenberg et al. 2017, Bif & Hansell 2019). The MLD was calculated using the same method as used in the model.

Satellite observations of 8 d chl *a* concentrations were obtained from the Copernicus-GlobColor products, which were merged with multiple observations, including observations from Sea-viewing Wide Field-of-View Sensor (SeaWiFS), Moderate-resolution Imaging Spectroradiometer (MODIS), Medium Resolution Imaging Spectrometer (MERIS), the Visible Infrared Imaging Radiometer Suite on the Suomi National Polar-orbiting Partnership & the Joint Polar Satellite System-1 (VIIRS-SNPP&JPSS1), and the Ocean and Land Color Imager on Sentinel-3 (OLCI-S3A&S3B). To be consistent with the BGC-Argo observations, these data were obtained for the whole year of 2012 for study. The spatial resolution of the global products is 4 km, and the monthly averaged time series is obtained by averaging the region centered at OSP within a  $2^\circ \times 2^\circ$  grid.

### 3. RESULTS

#### 3.1. BGC-Argo observed seasonal variability in ocean properties

After being deployed at OSP in February 2012, the BGC-Argo moved southeastward during the following year until January 2013 (Fig. 1a). Within this period, the distance between the float and OSP was consistently less than 200 km, and the bottom topography at the float location was approximately 4000 m. The seasonal variability in SCHL, which is captured by BGC-Argo observations at a depth of approximately 7 m, is consistent with satellite observations (Fig. 1b). In winter (January–March) and spring (April–June) the SCHL reaches its minimum of approximately  $0.2 \text{ mg m}^{-3}$ . The BGC-Argo observations of the chl *a* concentration within the mixed layer show a slight increase after April, but there is no significant increase in the depth-integrated chl *a* (ICHL) concentration from April to June. Therefore, the slight increase in chlorophyll within the mixed layer is considered to be caused by a reduction in dilution. The SCHL concentration begins to increase in July, reaching a distinct peak in September before decreasing in October and November. The SCHL observed by BGC-Argo exceeds  $0.6 \text{ mg m}^{-3}$ , which is within the variance of the satellite observations. This suggests that the chl *a* data captured by BGC-Argo are consistent with satellite data and are sufficiently representative to describe the seasonal variability in chl *a* at OSP.

The vertical profiles of temperature,  $\text{NO}_3$ , and chl *a* captured by BGC-Argo show prominent seasonal variability (Fig. 2a–c). In winter, the MLD reaches its

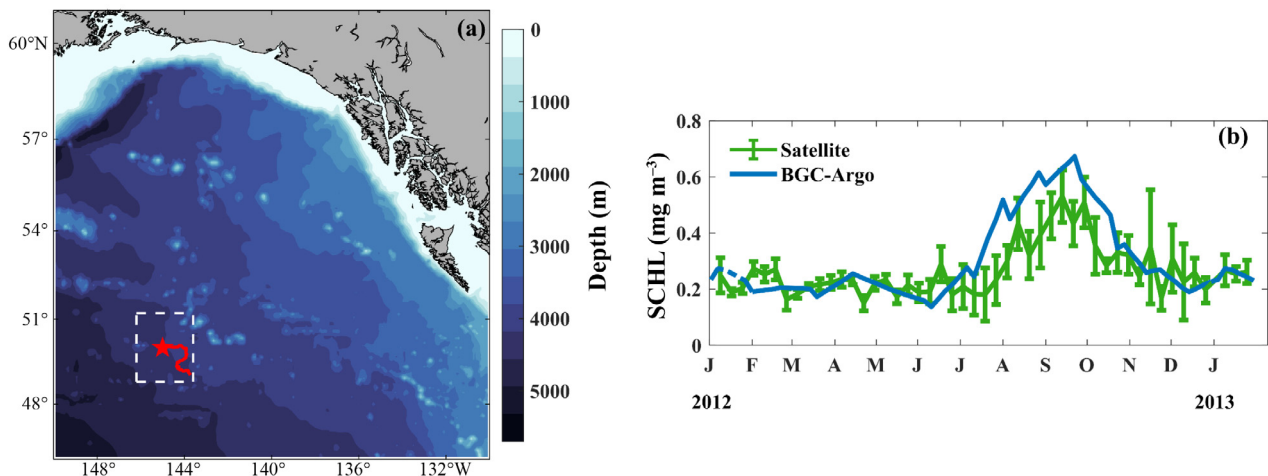


Fig. 1. (a) Biogeochemical Argo float (BGC-Argo, float ID: 7601StnP) location during the 1 yr deployment. Blue shading represents topography. Float track (red line) for BGC-Argo deployed at Ocean Station Papa (OSP; red star) in February 2012. (b) Time series of surface chlorophyll (SCHL) concentrations observed by satellite (green line) and by BGC-Argo (blue line). Satellite data were averaged in the area within the white dashed rectangle ( $49\text{--}51^\circ \text{N}$ ,  $151\text{--}149^\circ \text{W}$ ); error bars: spatial variance

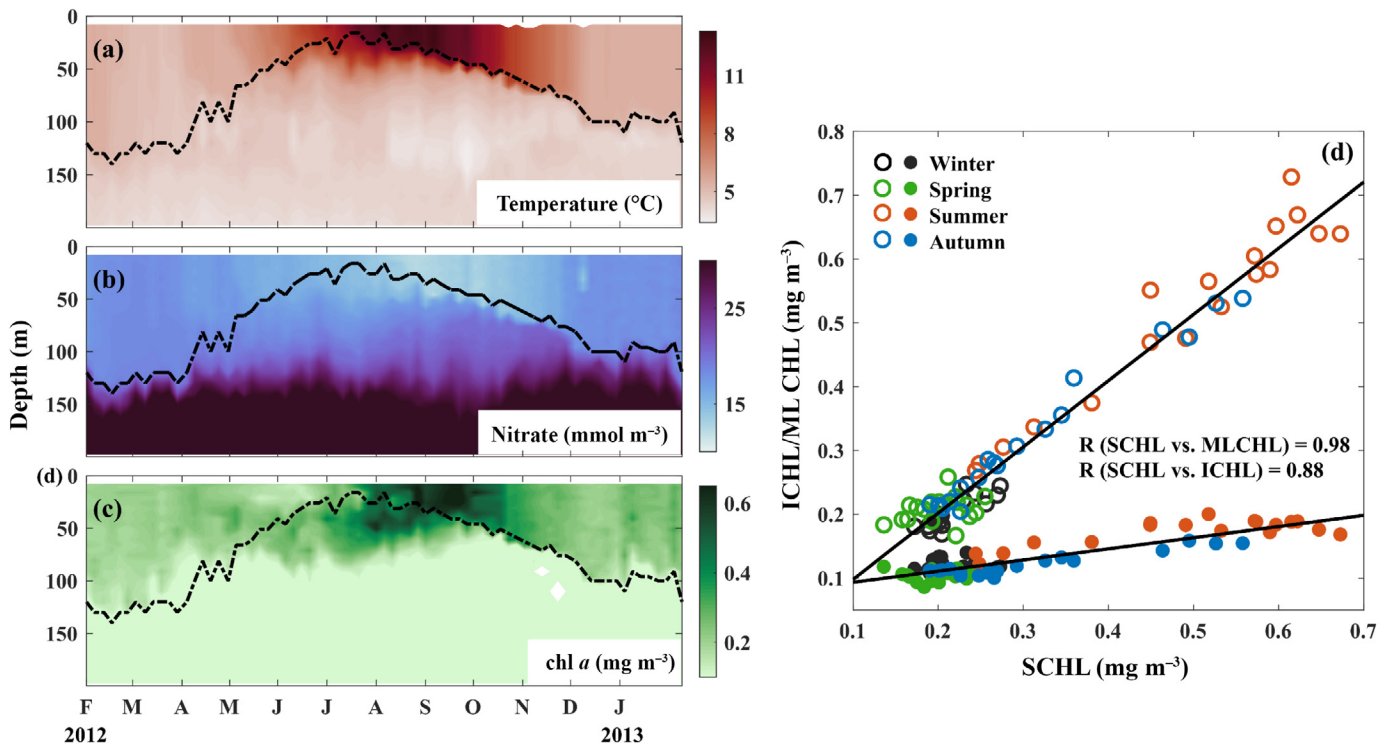


Fig. 2. (a–c) Water properties (temperature, nitrate, chl *a*) observed by BGC-Argo above 200 m. Black dashed line: mixed layer depth (MLD). (d) Surface chlorophyll (SCHL) versus depth-integrated (0–200 m) chlorophyll averaged within 200 m (ICHL; filled circles) and averaged chlorophyll in the mixed layer (MLCHL; open circles) at Ocean Station Papa. The correlation coefficients between surface chlorophyll and depth-integrated chlorophyll and between MLD and depth-integrated chlorophyll were significant at the 99.9% confidence level. Solid lines: linear regressions (SCHL vs. ICHL:  $y = 0.17x + 0.076$ ; SCHL vs. MLCHL:  $y = 1.038x - 0.0057$ )

maximum at approximately 140 m, and intense vertical mixing drives cold ( $5^{\circ}\text{C}$ ) and  $\text{NO}_3$ -rich ( $19 \text{ mmol m}^{-3}$ ) water into the mixed layer. As the MLD shoals after April, the surface water gradually warms and the  $\text{NO}_3$  concentration begins to decline; these processes are associated with a weak increase in chl *a* in the mixed layer. The increase in chl *a* is initiated at the subsurface (i.e. between 40 and 80 m) in June and continuously increases in the upper ocean until September. Simultaneously, the MLD shoals from April to July and deepens afterward, with its shallowest depth at approximately 15 m. The high chl *a* zone is usually limited within the mixed layer but extends to a depth greater than the MLD in June and July. In later summer and autumn (from August–October), as the sea surface temperature (SST) reaches its maximum of  $13^{\circ}\text{C}$  and  $\text{NO}_3$  reaches its minimum of  $13 \text{ mmol m}^{-3}$ , chl *a* peaks in the entire upper ocean, with a uniform value of approximately  $0.6 \text{ mg m}^{-3}$ . In addition, the vertical variation in chl *a* in the upper ocean is less prominent in all seasons except spring, when a subsurface increase in chl *a* can be identified. The SCHL is significantly corre-

lated with the average ICHL (between 0 and 200 m) ( $R = 0.88$ ) and with the average chl *a* in the mixed layer (MLCHL;  $R = 0.98$ ), while the slope of the linear regression for the latter is close to 1 (Fig. 2d). The high correlations indicate that the SCHL is highly representative of chl *a* in the upper ocean, which is consistent with previous cruise observations (Peña & Varela 2007).

### 3.2. Comparison between simulations and observations

The simulations of physical and biological factors in 2012 are compared with BGC-Argo observations at OSP (Fig. 3). Because the annual cycle is repeated in the model, the float observations in January 2012 are duplicated with the values in January 2013 to create a full-year period. The simulated seasonal patterns of SST (Fig. 3a) and MLD (Fig. 3b) are reasonably comparable with the BGC-Argo data (Fig. 3e). Although the minimum  $\text{NO}_3$  concentration in summer is lower in the model than in the observations

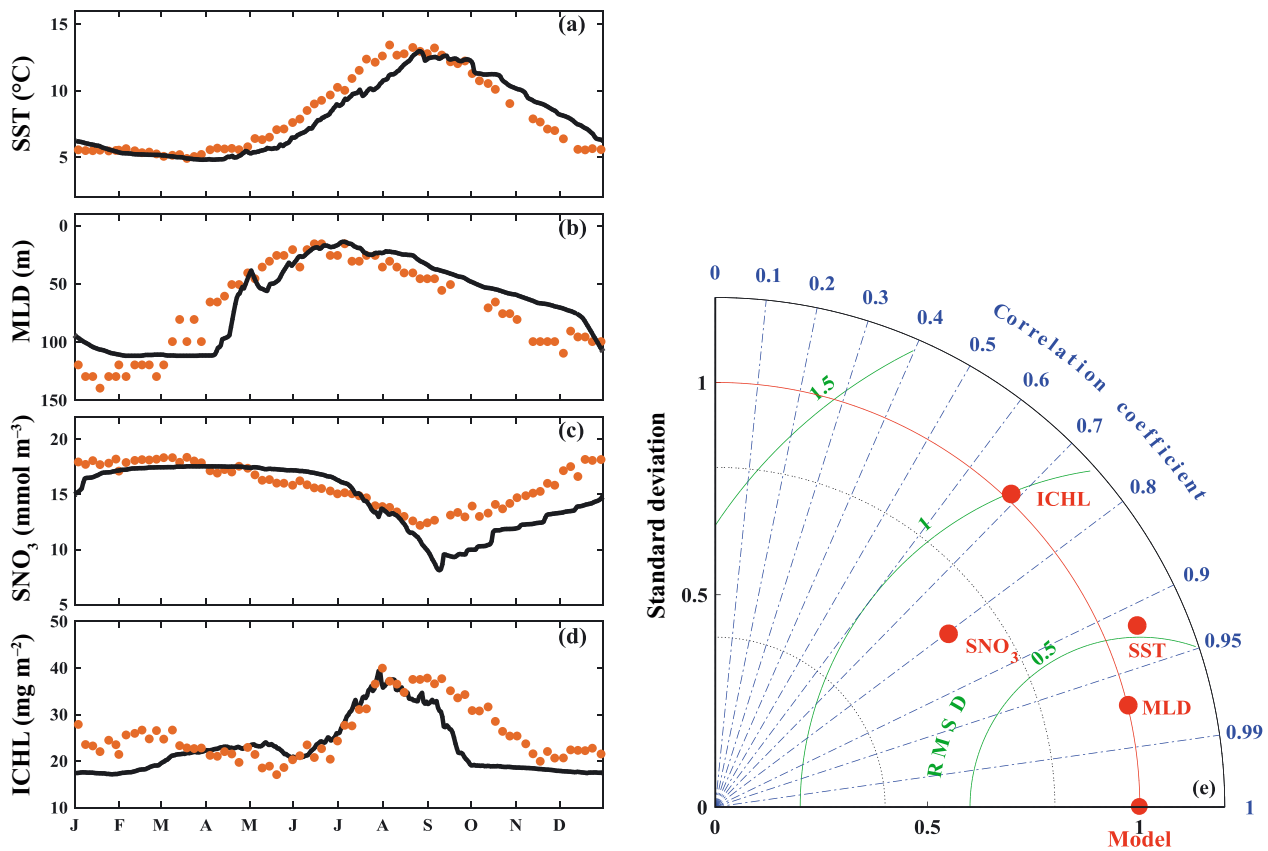


Fig. 3. Comparisons of simulated time series of (a) sea surface temperature (SST), (b) mixed layer depth (MLD), (c) surface nitrate (SNO<sub>3</sub>), and (d) averaged depth-integrated chlorophyll in the upper 200 m (ICHL) in 2012 with BGC-Argo float data. Orange solid circles: BGC-Argo float data; solid curves: model results. (e) Taylor diagrams demonstrating correlation coefficients, centered root-mean-square differences (RMSDs, in green), and normalized standard deviations of BGC-Argo-observed ICHL, SNO<sub>3</sub>, SST, and MLD with model data

(Fig. 3c), the simulated NO<sub>3</sub> concentration (~8 mmol m<sup>-3</sup>) is sufficient for the growth of phytoplankton. Thus, in the simulation, NO<sub>3</sub> has little influence on regulating seasonal variability in chl *a* at OSP, as suggested in previous studies (Westberry et al. 2016). Because chl *a* is uniformly distributed in the vertical direction, the ICHL is used to evaluate the performance of the model by comparing its modeled values with observations. Modeled ICHL begins to increase in July and maintains a relatively high value until September (Fig. 3d), which is associated with a decrease in the surface NO<sub>3</sub> concentration (Fig. 3c). This trend is in agreement with the observations. Note that the surface NO<sub>3</sub> concentration is used to gauge nutrient consumption, as the growth of phytoplankton takes place mainly in the upper part of the euphotic layer (Sigman & Hain 2012).

The correlation coefficients between the observations and the model data for SST, MLD, surface NO<sub>3</sub>, and ICHL are 0.92, 0.97, 0.80, and 0.69, respectively (Fig. 3e), and the associated root-mean-square differ-

ences (RMSDs) are 0.51, 0.23, 0.65, and 0.98, respectively. Overall, the model can reproduce the seasonal cycles of physical and biological factors observed by the BGC-Argo at OSP. Modeled chl *a* is less accurate than that of modeled temperature and MLD, which was due in part to the necessary simplification of the biogeochemical processes in the model.

The simulated vertical distribution of temperature, nutrients (e.g. NO<sub>3</sub> and dissolved Fe), and chl *a* are compared with observations at OSP in winter (February) and summer (August) (Fig. 4). The model reproduces the seasonal profile of temperature, chl *a*, and NO<sub>3</sub>, where chl *a* and NO<sub>3</sub> are uniformly distributed within the MLD in winter and vary monotonically with depth in summer. Due to the scarce data of dissolved Fe at OSP, the vertical distribution of dissolved Fe is only available between 0 and 1000 m in winter. Modeled dissolved Fe is comparable with the measurements except for dissolved Fe in the upper 100 m being higher than observations in the summer. The discrepancy between the simulated dissolved Fe

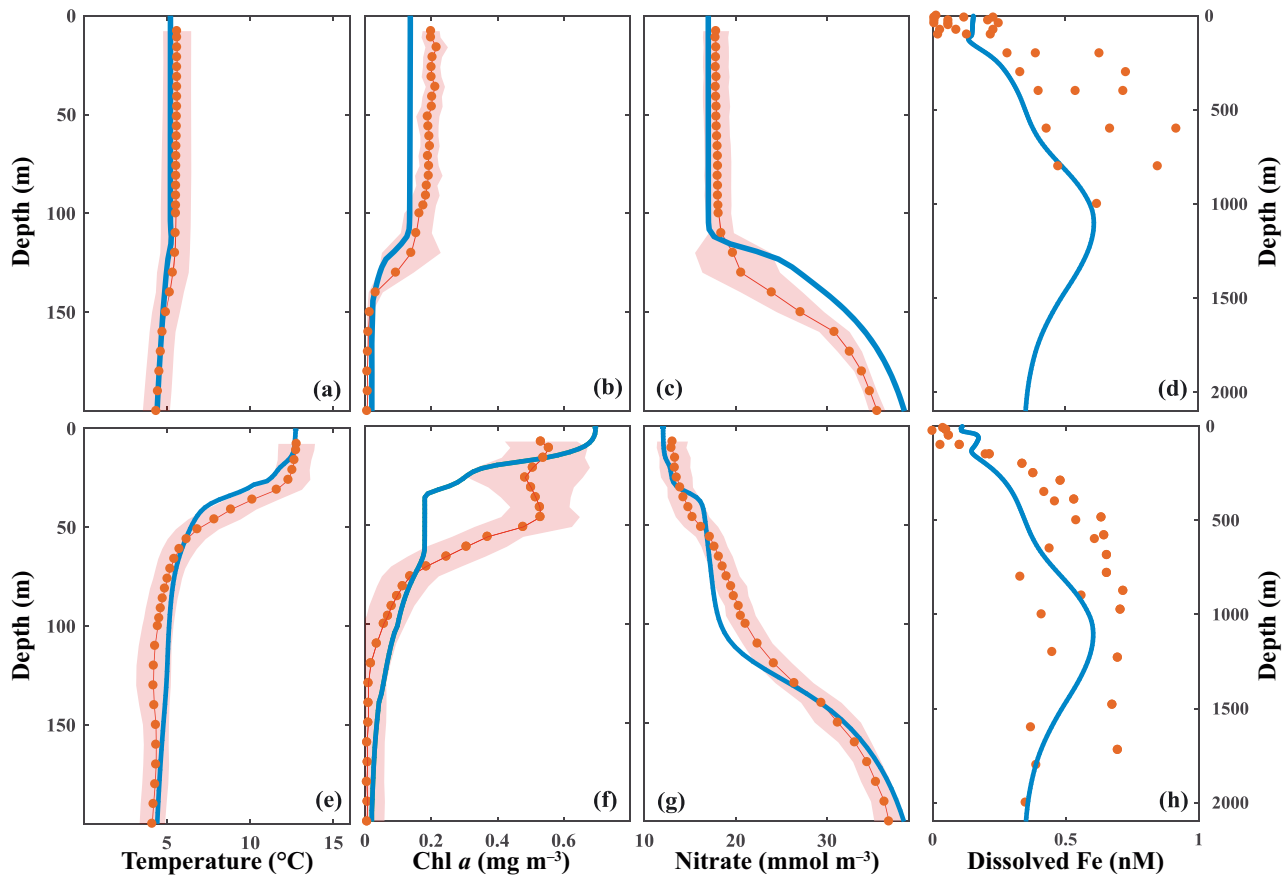


Fig. 4. Vertical profiles of (a) temperature, (b) chl *a*, (c)  $\text{NO}_3$ , and (d) dissolved Fe in February, and (e) temperature, (f) chl *a*, (g)  $\text{NO}_3$ , and (h) dissolved Fe in August. Blue solid curves: model results. (a,b,c,e,f,g) Red symbols: BGC-Argo observed monthly data; red shaded area: standard deviation of the BGC-Argo observed monthly data. (d,h) Red symbols: observed dissolved Fe from Tagliabue et al. (2012) (GEOTRACES data) and Schallenberg et al. (2015)

and chl *a* and the observations is probably due to not representing the process in which phytoplankton increase the absorption of Fe to improve the photosynthesis rate under low irradiance in the model, which could result in a slightly reduced dissolved Fe concentration and lower growth rate of phytoplankton under low irradiance. As a result, the simulated chl *a* in winter and chl *a* below the mixed layer in summer are lower than the observation due to the low-irradiance environment. A detailed discussion of the model accuracy is provided below.

The modeled depth-integrated primary production, water-column averaged phytoplankton growth rate, surface phytoplankton carbon, and mesozooplankton carbon in winter and summer are compared with reported literature values (Table 1). The seasonal variability of these model data compares well with that reported in prior studies, although lower primary production and phytoplankton biomass were identified in winter. This also occurred because the

model did not incorporate the process where phytoplankton absorb more Fe to improve their photosynthetic capacity under low-irradiance conditions. The modeled surface phytoplankton biomass in summer is set to simulate relatively high values to compensate for modeled lower growth rates at deeper depths in summer and reproduce the peak of the observed depth-integrated (0–150 m) primary production at OSP. Since there were no observed data of the zooplankton grazing rate, only the modeled zooplankton biomass was compared with observations. The modeled winter–summer variability of surface mesozooplankton biomass is larger than the result of Harrison (2002) but compares well with Boyd et al. (1995) (Table 1). The previous direct observations of microzooplankton that described the physiology of phytoplankton growth ( $\text{cells l}^{-1}$ ) cannot be compared with the model result ( $\text{mg C m}^{-3}$ ) due to different configurations. However, the seasonal variability of the observed microzooplankton concentration (winter:

Table 1. Comparison between model results and reported literature values in winter and summer

Parameter	Model result (winter–summer)	References (winter–summer)
Primary production ( $\text{mg C m}^{-2} \text{d}^{-1}$ )	82–690	150–450 to 300–1500 (Boyd & Harrison 1999), 300 to 400–850 (Wong & Mearns 1999, Harrison 2002)
Growth rate of phytoplankton ( $\text{d}^{-1}$ )	0.07–0.4	0.07–0.3 to 0.3–0.8 (Boyd & Harrison 1999)
Surface phytoplankton carbon ( $\text{mg C m}^{-3}$ )	5–45	15 to 25 (Harrison 2002), <10 to ~32 (Westberry et al. 2016)
Surface mesozooplankton carbon ( $\text{mg C m}^{-3}$ )	0.7–51	0.3–1.3 to >35 (Boyd et al. 1995), 3 to 20 (Goldblatt et al. 1999, Harrison 2002)

2.9–15.3  $\text{l}^{-1}$ ; summer: 14.6  $\text{l}^{-1}$ ; Boyd et al. 1995) is smaller than that of mesozooplankton (Harrison et al. 2004), which agrees well with model results.

### 3.3. Factors controlling seasonal variation in phytoplankton

The factors in the model—i.e. surface photosynthetically active radiation (PAR), surface BFe concentration, and depth-integrated microzooplankton biomass—are compared with the depth-integrated biomass of small phytoplankton and diatoms to illustrate the seasonal variability in chl *a* (Fig. 5). The dia-

tom biomass is much lower than the small phytoplankton biomass throughout the year, indicating that the ICHL is dominated by small phytoplankton (Fig. 4b). The depth-integrated small phytoplankton biomass and the biological fluxes are intentionally applied in the current study to investigate seasonal variability in chl *a*. Consistent with the observed seasonal cycle of dissolved Fe (Harrison 2002), simulated surface BFe is higher in winter than in summer (Fig. 4d,h). BFe increases from winter to spring until reaching its maximum concentration (~0.18 nM) in June. However, the small phytoplankton biomass increases slightly but remains at a low value (<10  $\text{mmol N m}^{-2}$ ) during the same period, indicating that the growth of small phytoplankton is not limited by BFe and is due to the increase in surface PAR, especially in early March. Instead, the biomass of overwintering microzooplankton increases quickly in March, which is associated with minimal increases in the small phytoplankton biomass. Subsequently, as the small phytoplankton biomass reaches the threshold for microzooplankton grazing, there is an increase in microzooplankton due to grazing on small phytoplankton, which cannot prominently increase until June when the MLD is shallow enough to allow the small phytoplankton growth to overcome microzooplankton grazing. The small phytoplankton biomass rapidly increases starting in June, when surface PAR is high, which results in a decrease in BFe. The increase in small phytoplankton biomass lasts until August, and it remains relatively high (>20  $\text{mmol N m}^{-2}$ ) until September; this is much later than the peak surface PAR that occurs in July. The microzooplankton biomass always increases following the increase in small phytoplankton biomass, but it starts to decrease in mid-July when the small phytoplankton biomass is still increasing, which

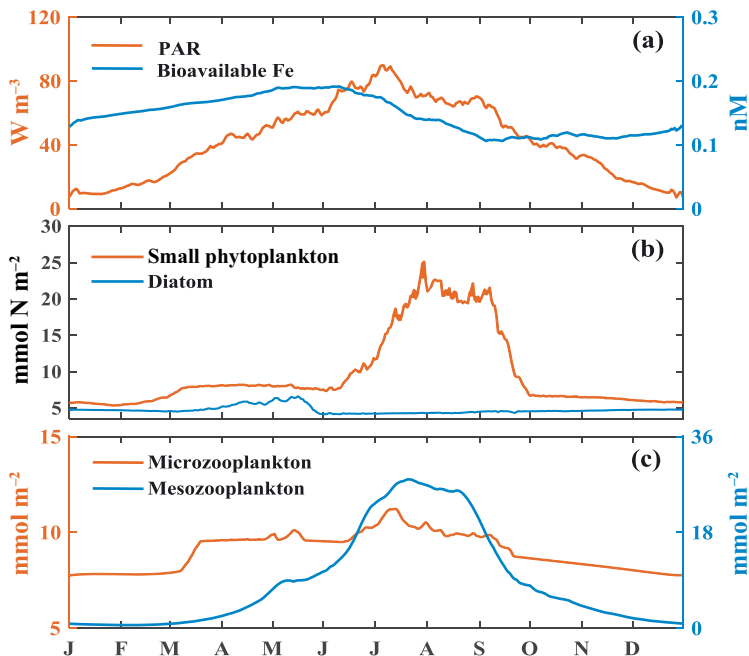


Fig. 5. Modeled 1 yr time series of (a) surface photosynthetically active radiation (PAR) and bioavailable Fe (BFe) concentration, (b) depth-integrated small phytoplankton and diatom biomass, and (c) depth-integrated microzooplankton and mesozooplankton biomass

is considered to be controlled by mesozooplankton (Fig. 5c). Thus, the early decline in microzooplankton biomass reduces microzooplankton grazing, which helps maintain high levels of small phytoplankton biomass in August and September (Fig. 5b). After October, the loss term—e.g. remineralization of microzooplankton, remineralization, and aggregation of small phytoplankton that are proportional to their respective biomass—controls the variation in microzooplankton and small phytoplankton biomass. As a result, the depth-integrated small phytoplankton and microzooplankton biomass rapidly decrease.

The change in phytoplankton biomass in the model is determined simultaneously by physical processes (e.g. vertical mixing and sinking) and biological processes (e.g. phytoplankton growth, remineralization, aggregation, and zooplankton grazing). Phytoplankton growth represents the primary production of phytoplankton, which utilize nutrients and light to photosynthesize. To further illustrate the influence of these processes on the seasonal variability in small phytoplankton biomass, the depth-integrated (0–200 m) nitrogen budget of each process was compared (Fig. 6a). Due to the role of microzooplankton biomass in affecting small phytoplankton biomass, the depth-integrated (0–200 m) nitrogen budget of each process of microzooplankton is also shown (Fig. 6b). Because the magnitudes of depth-integrated sinking and vertical mixing are close to zero (especially that of the latter, which affects only the vertical distribution of phytoplankton and contri-

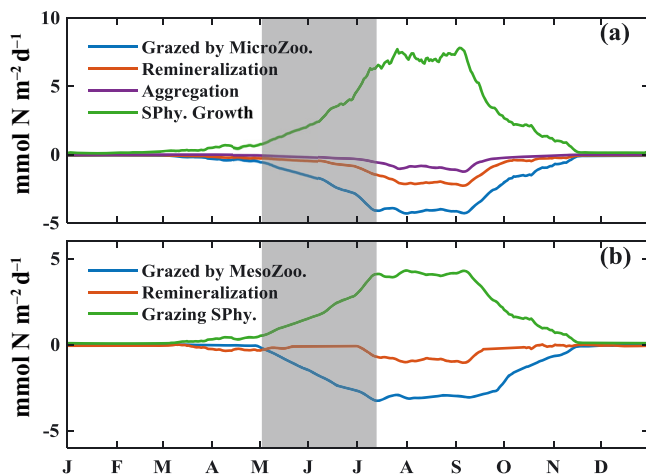


Fig. 6. Modeled time series of vertically depth-integrated nitrogen (a) grazed by microzooplankton (MicroZoo.), remineralization, aggregation, and growth of small phytoplankton (SPhy.) and (b) grazed by mesozooplankton, remineralization, and growth of microzooplankton (grazing on small phytoplankton). Gray area: the period when microzooplankton grazing rapidly increases from May to mid-July

butes little to total phytoplankton biomass in the water column), these 2 processes are not shown in the figure. In winter, all biological fluxes are generally small. The increase in small phytoplankton growth takes place in May together with an increase in the loss terms, i.e. remineralization, aggregation, and microzooplankton grazing. This is because the magnitudes of the loss terms depend on the concentration of small phytoplankton, especially the magnitude of microzooplankton grazing, which increases more quickly than those of the other 2 loss terms. In addition, microzooplankton grazing depends on the concentration of microzooplankton and small phytoplankton, both of which are high in May, resulting in high grazing rates. The overwintering microzooplankton, which show less grazing by mesozooplankton in spring (Fig. 6b), have a relatively high grazing capability and slow the spring increase in small phytoplankton growth, leading to a slow increase in small phytoplankton biomass until July, but the increase in small phytoplankton biomass before July is due mainly to the co-effect of temperature, light, and nutrients (Fig. 6a).

The factors controlling the change in small phytoplankton growth are investigated (Fig. 7) using the phytoplankton SGR, which is defined as the ratio between phytoplankton growth and phytoplankton

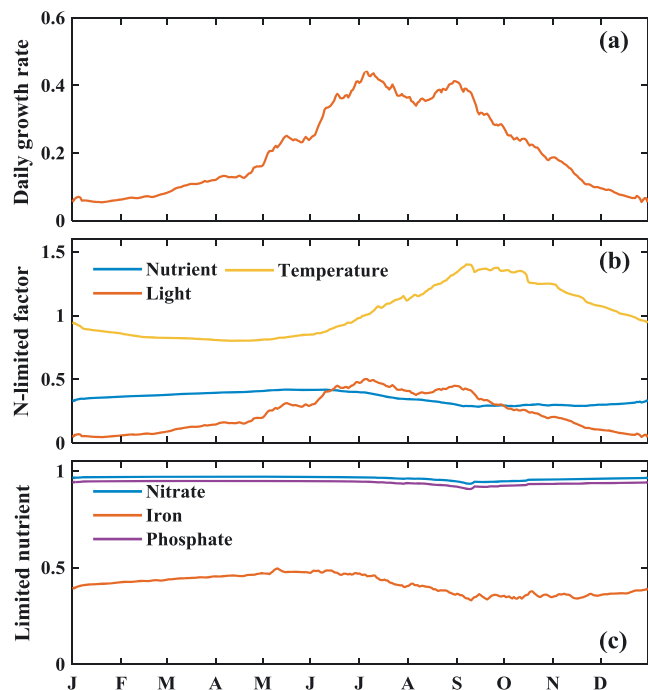


Fig. 7. Modeled time series of the vertically integrated (a) growth rate, (b) dominant limiting factor, and (c) limiting nutrient factor for small phytoplankton weighted by the small phytoplankton biomass

biomass. The SGR of small phytoplankton is vertically integrated and weighted by the corresponding small phytoplankton biomass instead of depth integration (Fig. 7a). This vertical integration weighting by the small phytoplankton biomass incorporates the influence of changes in the MLD on SGR and shows the summer SGR within the water column (Fig. S3). The monthly time series of the SGR is also characterized by a prominent seasonal cycle, with high values in summer between June and September (approximately  $0.4 \text{ d}^{-1}$ ) associated with a rapid increase in phytoplankton biomass. In contrast, the winter SGR shows relatively low values between November and April (approximately  $0.07 \text{ d}^{-1}$ ) (Fig. 5b). The simulation data are consistent with previous observations in which the observed SGR in winter ( $<0.1 \text{ d}^{-1}$ ) is much lower than that in summer ( $0.3\text{--}0.9 \text{ d}^{-1}$ ) (Boyd & Harrison 1999).

The SGR of small phytoplankton is the product of 3 regulating factors, i.e. nutrients, temperature, and light. Thus, for a single regulating factor, a high value indicates that it is favorable to the growth of small phytoplankton. The SGR of small phytoplankton clearly follows the temporal variation in light, particularly during the period before July. Specifically, both light and SGR are extremely low in winter and increase slowly until May, suggesting that light substantially limits ( $\sim 0.05$ ) the growth of small phytoplankton (Fig. 7b). Simultaneously, a deep MLD can reduce the effective light available by mixing the phytoplankton downward into deep water, where there is insufficient light (Plant et al. 2016). A large increase in the growth rate occurs in June (Fig. 7a) because shoaling of the mixed layer weakens light limitation (Fig. 3b), and temperature and light both increase (Fig. 7b). The SGR remains high from July to August as temperature and light limitations are alleviated by the shallow MLD, resulting in greater nutrient utilization (Figs. 3c & 5a). The reduction in nutrients, i.e. Fe (Fig. 3a), induces stronger nutrient limitation in summer that, in turn, reduces the maximum SGR. This process was considered to prevent the occurrence of the phytoplankton blooms that occur regularly in the western North Pacific Ocean, as a shallow mixed layer increases light availability (Matsumoto et al. 2014). Nutrient limitation depends on the minimum levels of the limiting nutrients (i.e.  $\text{NO}_3+\text{NO}_4$ ,  $\text{PO}_4$ , and BFe) for small phytoplankton. The model results reveal that Fe limitation dominates the nutrient limitation for the phytoplankton growth rate throughout the year (Fig. 7c). Limitations in nutrients, light, and temperature occur simultaneously in September and are associated with the

deepening of the MLD and a dramatic decrease in the SGR (Fig. 6a). Note that light limitation becomes the dominant limiting factor for small phytoplankton growth again in winter and remains dominant through the following spring.

In addition to phytoplankton growth, microzooplankton grazing also plays a role in determining the biomass of small phytoplankton. The period shaded in gray in Fig. 6 represents the time span when microzooplankton grazing rapidly increases from May to mid-July, after which the value remains stable. The period is shorter than the period with increased small phytoplankton growth, which lasts until August. In contrast to the stable value of microzooplankton grazing ( $\sim -4.32 \text{ mmol N m}^{-2}$ ), small phytoplankton growth, remineralization, and aggregation continue to increase (Fig. 6a). This suggests that the removal of microzooplankton biomass (Fig. 5c) starting in early July reduces microzooplankton grazing and facilitates an increase in small phytoplankton biomass (Fig. 5b); this increase leads to phytoplankton growth reaching its maximum ( $\sim 8 \text{ mmol N m}^{-2} \text{ d}^{-1}$ ) in August, despite the decrease in the SGR of phytoplankton. Although there is plenty of food (i.e. small phytoplankton) for microzooplankton from July to August, their biomass actually decreases. This is mainly related to mesozooplankton grazing, which is the major loss term for microzooplankton ( $\sim -3.14 \text{ mmol N m}^{-2} \text{ d}^{-1}$ ) (Fig. 6b). Microzooplankton grazing remains low until September, which helps to maintain the high concentration of small phytoplankton during this period.

## 4. DISCUSSION

### 4.1. Mechanisms controlling the seasonal variability of phytoplankton

A BGC-Argo deployed at OSP increased the temporal resolution of the observations throughout the year and expanded the sampling period of previous cruise observations (Plant et al. 2016, Westberry et al. 2016). The float observations provide comprehensive insight into the seasonal cycle of biochemical factors and were applied in the current study to develop a 1D physical–biochemical coupled model. The model successfully reproduces the physical and biogeochemical conditions observed by the BGC-Argo (Figs. 3 & 4). Model simulations are used to further investigate the seasonal dynamics of phytoplankton in the SNEP. Earlier studies showed that the seasonal variability in phytoplankton biomass was determined by multiple control factors, e.g. mixing, light availability, nutrient

limitation, and zooplankton grazing (Letelier et al. 2004, Behrenfeld 2010, Taylor & Ferrari 2011). The impact of mixing on phytoplankton is particularly important in regions where the MLD in winter is shallower than the euphotic zone depth, where PAR is reduced to 1% of its surface value throughout the year and surface phytoplankton growth is limited by macronutrients in other seasons, resulting in a subsurface chl *a* maximum (Geng et al. 2019). The enhanced vertical mixing in winter leads to an upward displacement of NO<sub>3</sub>-rich water that elevates the chl *a* level within the entire MLD and leads to a peak value of SCHL, in contrast to the subsurface chl *a* maximum that occurs in other seasons (Geng et al. 2019). This mechanism allows phytoplankton to grow fast as soon as they have enough nutrients. Although deep mixing in winter leads to increased NO<sub>3</sub> and dissolved Fe at OSP, the chl *a* remains low in spring when the MLD becomes shallower. This suggests that the enhancement in dissolved Fe due to winter mixing is too weak to rapidly elevate phytoplankton growth, which is in contrast to the spring bloom in the western subarctic Pacific, where the dissolved Fe is much higher than that in the eastern subarctic Pacific (Harrison et al. 2004, Nishioka et al. 2020). However, observations from both cruise and BGC-Argo data, together with the model simulations, showed little vertical variation in chl *a* at OSP throughout the year; the peak chl *a* occurred in late summer when the MLD was shallowest (Boyd & Harrison 1999, Peña & Varela 2007, Schallenberg et al. 2017). Thus, the mixing mechanism described in other studies is not applicable to the region near OSP. Another mixing-related mechanism can occur when the MLD becomes deeper than the euphotic layer (Matsumoto et al. 2014). Strong winter mixing distributes phytoplankton evenly within the deep MLD, and the phytoplankton beneath the euphotic layer receive limited light for growth. Consistent with this process, the model in this study captures a similar process at OSP in which strong vertical mixing extends deeper than the MLD and leads to a strong light limitation on phytoplankton growth in winter (Fig. 7b). Due to the changes in the MLD, light availability within the mixed layer, rather than surface irradiance, controls the temporal evolution of phytoplankton growth (Matsumoto et al. 2014). Therefore, simulated small phytoplankton growth remains at a low level from January to May, despite the corresponding surface PAR increasing by 5-fold (Figs. 5a & 6a). Small phytoplankton growth then increases rapidly until July because of mixed layer shoaling.

Observations in previous studies revealed that phytoplankton under low light irradiance increase

their demand for BFe, which is used to synthesize light-harvesting pigments and Fe-containing redox proteins that are involved in photosynthesis (Sunda & Huntsman 1997). These extra pigments and proteins help phytoplankton maintain a high photosynthesis rate when light irradiance is low (Maldonado et al. 1999). However, this process is not incorporated in the current model; thus, simulated phytoplankton growth is reduced when there is low light availability. This can help to explain the lower simulated ICHL value in winter compared with the observed ICHL value (Fig. 3d). It is important to emphasize that the underestimation of phytoplankton growth in winter does not interfere with the accuracy of the simulated role of light in regulating phytoplankton biomass from winter to summer. For instance, a similar relationship between light and phytoplankton growth has been confirmed in the subarctic north-west Pacific Ocean (SNWP) (Sasai et al. 2016). The high dissolved Fe concentration in winter cannot overcome the impact of light limitation on phytoplankton growth (Harrison et al. 2004), indicating that the increased demand for BFe is less influential than light in simulations of the seasonal cycle of phytoplankton growth.

In contrast to the SNEP, a remarkable phytoplankton bloom has been identified in the SNWP, where Fe is abundant (Mochizuki et al. 2002, Fujiki et al. 2014). This bloom is mostly triggered by the increase in light availability when the MLD shoals (Matsumoto et al. 2014). The model results show that after MLD shoaling, both Fe limitation and microzooplankton grazing impact the growth of phytoplankton biomass after the increase in light availability at OSP (Fig. 6a,c). Chl *a* has not increased dramatically at OSP. The underlying mechanisms of phytoplankton growth are further evaluated by conducting sensitivity experiments, in particular to quantify the influence of Fe limitation and microzooplankton grazing on the growth of phytoplankton (Fig. 8). If the microzooplankton did not survive the winter, i.e. if the impact of microzooplankton grazing in spring were eliminated by reducing the threshold of mesozooplankton grazing on microzooplankton to zero (Expt 1), the increase in the SCHL would start in April, as in the SNWP. By amplifying the Fe input from dust deposition by 1.5 times (Expt 2) to increase the BFe in the model, the value of SCHL becomes double that in the control run, though the seasonality is highly consistent. As the Fe input is further increased, i.e. by 2.5 times (Expt 3), the SCHL increases greatly, and the bloom period is earlier than in the control run, i.e. maintaining the peak value

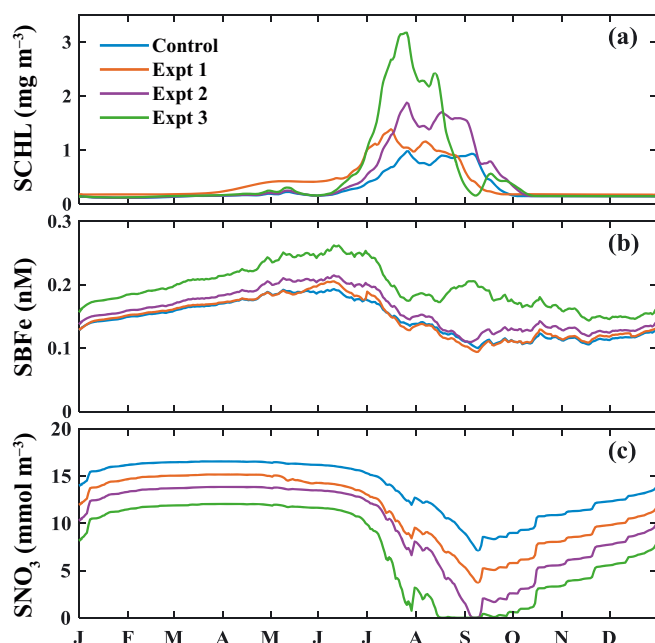


Fig. 8. Modeled 1 yr time series of (a) surface chl *a* (SCHL), (b) surface bioavailable Fe (SBFe), and (c) surface nitrate concentrations ( $\text{SNO}_3$ ) for the control, Expt 1 (sensitivity experiment with no zooplankton stock in winter), Expt 2 (with 1.5 times the dissolved Fe [deposition]) and Expt 3 (with 2.5 times the dissolved Fe deposition)

until July. In all 3 experiments, the peak of chl *a* increases to more than  $1 \text{ mg m}^{-3}$ , which corresponds to the magnitude of chl *a* during the spring bloom in the SNWP (Matsumoto et al. 2014). Thus, the region around OSP lacks a spring phytoplankton bloom because of both the scarcity of BFe and grazing pressure from overwintering microzooplankton (Martin & Fitzwater 1988, Miller et al. 1991, Marchetti et al. 2006). The simulated peak chl *a* in the SNEP still occurs 1 to 2 mo later than that observed in the SNWP; this is in part because the initiation of mixed layer shoaling in the SNEP occurs 2 mo later than in the SNWP (Harrison et al. 2004). The SCHL between April and mid-June is higher in Expt 1 than in Expts 2 and 3, suggesting that microzooplankton grazing on chl *a* is more important than Fe limitation during the period when light limitation dominates phytoplankton growth (Fig. 7b). As light limitation is alleviated after June, Fe limitation on phytoplankton growth becomes more prominent. In July, mean surface BFe increases from 0.15 to 0.17 nM in Expt 2 and to 0.21 nM in Expt 3 (Fig. 8b). The corresponding increases in SCHL in Expts 2 and 3 reach 2 and  $3 \text{ mg m}^{-3}$ , respectively (Fig. 8a) and are associated with the depletion of surface  $\text{NO}_3$  (Fig. 8c). This result is

consistent with previous Fe-enrichment experiments showing that adding Fe results in a larger increase in chl *a* in summer than in winter because of the stronger Fe limitation in summer (Boyd et al. 1996, Harrison et al. 2004). This result also suggests that the increase in chl *a* induced by the weakening of Fe limitation is more significant than that induced by the removal of overwintering microzooplankton. It is important to point out that in the case without Fe limitation, instead of simply amplifying the Fe input from dust deposition, the modeled diatom biomass increases rapidly and peaks earlier than for small phytoplankton, introducing a spring bloom of phytoplankton (Figs. S4 & S5).

In previous cruise observations, the observed peak of chl *a* in late summer at OSP was generally attributed to increased light availability (Harrison et al. 2004). However, the BGC-Argo observations reveal that the high concentration of chl *a* can last until September, when the light has already begun to decrease (Figs. 3d & 4a). Consistent with these observations, the model reproduces the high level of small phytoplankton biomass that is maintained from August to September (Fig. 5b) because of the removal of microzooplankton (Fig. 5c) and the temperature being appropriate for phytoplankton growth (Fig. 7c). Previous studies attributed the high chl *a* in autumn to both the nutrient supply from enhanced vertical mixing and the decrease in zooplankton grazing (Findlay et al. 2006, Matsumoto et al. 2014). By incorporating the effects of both light and Fe, the simulation reveals that the growth rate of small phytoplankton reaches a maximum value in July and slightly decreases until August (Fig. 7), while the small phytoplankton growth is maintained at approximately the peak value in August (Fig. 6a). Thus, the high biomass of small phytoplankton from August to September is accompanied by a decrease in the growth rate, indicating the importance of the loss of microzooplankton grazing (Figs. 6 & 7). In line with these findings, a significant increase in chl *a* was also observed in September at the SNWP, which is dominated by small phytoplankton with much higher chl *a* levels than those at OSP due to the loss of grazing pressure from microzooplankton (Fujiki et al. 2014). To further quantify the role of microzooplankton grazing in fostering the biomass peak for small phytoplankton in summer, the net SGR (Fig. 9a), together with the growth, grazing, remineralization, and aggregation of small phytoplankton, are investigated from June to October (Fig. 9b). Here, net SGR equals the growth minus loss terms, i.e. grazing, remineralization, and aggregation. The positive net SGR indicates an in-

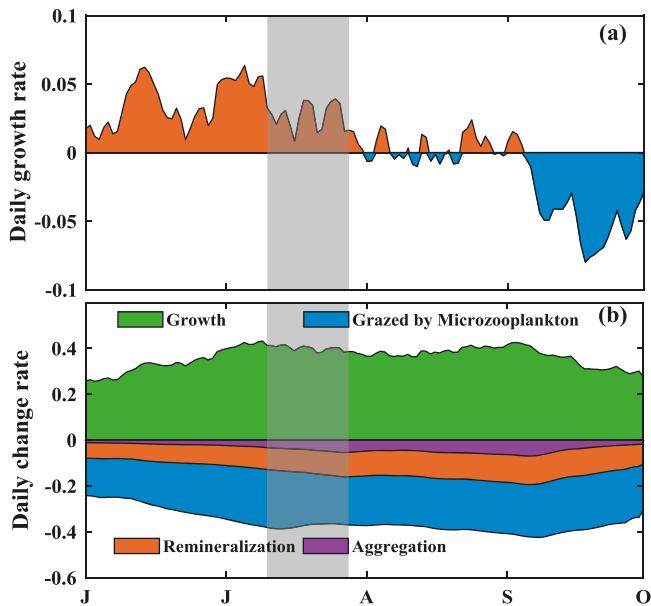


Fig. 9. Modeled time series of the vertically integrated specific rates of (a) net growth (orange: positive; blue: negative), and (b) remineralization, aggregation, grazing by microzooplankton, and growth rate of small phytoplankton. Gray area: the period from the peak specific microzooplankton grazing rate in early July to the time when it stops decreasing at the end of July

crease in the small phytoplankton biomass. The gray area in Fig. 9 represents the period from the peak specific microzooplankton grazing rate in early July to the time when it stops decreasing, i.e. at the end of July. Due to the intensified light and Fe limitations, the SGR slightly reduces from  $0.41 \text{ d}^{-1}$  at the beginning of July to  $0.38 \text{ d}^{-1}$  at the end of July (gray area in Fig. 9a), and the specific grazing rate decreases from  $0.25$  to  $0.20 \text{ d}^{-1}$ ; in addition, the other 2 loss terms, i.e. remineralization and aggregation, increase from  $0.095$  and  $0.032 \text{ d}^{-1}$  to  $0.11$  and  $0.053 \text{ d}^{-1}$ , respectively. Therefore, in July, the SGR and specific grazing rate decrease by 7.32 and 20%, respectively. As a result, the net SGR remains low but positive ( $\sim 0.03 \text{ d}^{-1}$ ) at the end of July. The loss of microzooplankton grazing is related to rapid grazing on microzooplankton by mesozooplankton before the small phytoplankton biomass peaks, leading to a reduction in grazing pressure on small phytoplankton from August to September (Fig. 6b). The simulation is highly consistent with previous observations that the mesozooplankton biomass peaks in summer at OSP (Timothy et al. 2013), indicating that the reduction in microzooplankton grazing plays an important role in maintaining the high small phytoplankton biomass from August to September.

## 4.2. Assessing the uncertainties in the model

There are 2 profiling floats (float 7601StnP and float 6400StnP) equipped with a fluorometer sensor which can measure chl *a* deployed at OSP. Because there are substantial missing chl *a* data in the upper ocean for float 6400StnP and it is necessary to minimize the influence induced by spatial differences in the selection of observation data, the ocean properties observed by float 7601StnP in 2012 are compared with the model results to evaluate the accuracy of the model. Though an intense aerosol deposition event from Siberian forest fires was encountered at OSP, it did not influence dissolved Fe concentrations in surface waters or oceanic primary production (Schallenberg et al. 2017). Additionally, the seasonal variability in the physical and biogeochemical environmental conditions, i.e.  $\text{NO}_3$ , oxygen, and particle backscatter coefficients, based on merged observations from multiple BGC-Argo areas around OSP from 2008 to 2015 was almost identical to that in 2012, and the slight difference in the peak time of these variables was considered to be caused by the location of the float (Plant et al. 2016). Furthermore, the observation studies of a previous cruise have shown higher chl *a* at OSP in late summer ( $0.2 \text{ mg m}^{-3}$  in winter,  $0.4$  to  $0.6 \text{ mg m}^{-3}$  in summer) (Harrison 2002, Peña & Varela 2007). This suggests that the 2012 BGC-Argo data are highly representative of the seasonal variability around OSP and do not include extreme events or interannual variability in biological features. Therefore, the seasonal dynamics of phytoplankton can be investigated by reproducing the physical and biogeochemical parameters observed by the BGC-Argo with the numerical model. Please note the MODIS observed summer chl *a* of climatology is lower than that of 2012 (Fig. S6) and only the BGC-Argo observation in 2012 is used to validate the model, which may potentially influence describing the seasonal phytoplankton dynamics.

The 1D model applied in the current study does not include advection and mesoscale processes, such as eddies, that can transport nutrients from the continental margin into the open ocean, i.e. the Gulf of Alaska (Johnson et al. 2005, Lam et al. 2006). However, OSP is located very far from the coast, where horizontal advection-induced coastal inputs, i.e. those from major rivers and coastal upwelling, are minimal (Kawamiya et al. 1995, Whitney et al. 1998). Furthermore, the mesoscale eddies in the Gulf of Alaska occur sporadically, without a prominent seasonal pattern, especially in the deep basin around OSP (Cummins & Lagerloef 2004, Jackson et al. 2006). The input

of nutrients, e.g. Fe, from mesoscale eddies can occasionally influence the variability of biogeochemical processes at OSP, but it contributes little to seasonal variability (Peña & Varela 2007). Thus, although horizontal advection and mesoscale processes are ignored in the 1D model in the interest of simplicity, it is still applicable for investigating seasonal phytoplankton dynamics at OSP. Compared with coarse-resolution 3D models, a 1D model with high vertical resolution is better able to represent phytoplankton dynamics within the upper mixed layer (Geng et al. 2019).

The seasonal variability in chl *a* reproduced by the 1D model in this study is highly consistent with the BGC-Argo observations, although the simulated chl *a* in winter is lower than the observed chl *a* and the simulated chl *a* in summer in a shallower layer is higher than the observed (Figs. 3d & 4f). This is in part because phytoplankton absorb more Fe to improve their photosynthetic capacity under low-irradiance conditions (Sunda & Huntsman 1997), but this process is not incorporated in the model. As a result, the model could reproduce the actual phytoplankton growth rate under high irradiance. However, under low irradiance, the simulated phytoplankton growth rate will be lower than that in reality, leading to a lower chl *a* in winter and below the mixed layer in summer (Figs. 3d, 4f & 5a). In addition, the lack of this process would lead to slightly redundant BFe because of the reduced phytoplankton uptake of BFe. However, the seasonal cycle of simulated surface BFe is consistent with observations, e.g. the simulated surface BFe in summer is not exhausted ( $\sim 0.09$  nM), equaling nearly half of that in winter ( $\sim 0.16$  nM). It is in a reasonable range compared with the observed seasonal cycle of dissolved Fe in previous studies, where the summer concentration ( $\sim 0.05$  nM) is also half that in winter ( $\sim 0.1$  nM) (Harrison 2002). Furthermore, the spring and summer BFe supply in the upper ocean includes exchange between BFe and inert Fe, e.g.  $\text{Fe}_{\text{Col}}$  and Fe in lithogenic particles, in addition to dust deposition. The conversion of inert Fe to BFe is related to photoreduction, which increases the BFe under higher light conditions (Rijkenberg et al. 2005), which is incorporated in the model. In addition, the conversion flux from inert Fe to BFe in the model also includes the remineralization of plankton debris, which could increase the flux from inert Fe to BFe, leading to an increase in BFe when phytoplankton biomass is high (Lee & Fisher 1993). The conversion flux from inert Fe to BFe is therefore the highest during summer and replenishes the lost BFe that was absorbed by phytoplankton growth. Thus, the Fe limitation for phytoplankton growth is slightly stronger in

summer than that in winter (Fig. 7c). Therefore, the flux of inert Fe that is converted to BFe is highest during summer, when there is enough light. Simultaneously, it can replenish the loss of BFe absorbed by phytoplankton growth, resulting in a surplus of BFe in summer (Fig. S7). To compensate for the model deficiency, the Fe cycle in the model was initialized by the profile of observed total dissolved Fe, including the  $\text{Fe}_{\text{Col}}$ , Fe-binding ligands, and labile inorganic Fe (Gledhill & Buck 2012). Because there are no publicly available observations of the different Fe components at OSP, the ratio measured in the western Pacific was applied to improve the accuracy of the model in describing Fe components, following Xiu & Chai (2021). It is important to point out that there are large spatial variations in Fe-binding ligand concentrations in the global ocean (Gledhill & Buck 2012) that are not considered in the current study. These factors can result in large uncertainties in reproducing the Fe cycle and describing its impact on the growth of phytoplankton. Further observations at OSP are required to characterize the Fe speciation and describe the ligand concentration, which will be important for the development of a comprehensive and accurate model.

The decrease in mesozooplankton grazing during winter was found to be related to their dormancy, which takes place in deep layers during winter (Miller & Clemons 1988, Harrison et al. 2004). Therefore, microzooplankton and diatoms would not be grazed in the upper ocean during winter. To simulate the process when the mesozooplankton grazing terminates in winter, a threshold for mesozooplankton grazing on microzooplankton and diatoms was incorporated in the model, and the threshold was adjusted to reproduce the time series of BGC-Argo observed ICHL (Fig. S8) and the seasonal cycle of microzooplankton following previous studies (Boyd et al. 1995). Because the model did not incorporate the process where phytoplankton absorb more Fe to improve their photosynthetic capacity under low-irradiance conditions, the relatively lower value of simulated ICHL in winter than that observed would be in a reasonable range. The physiology of phytoplankton can be parameterized and applied in the model for further improvements in the future.

## 5. CONCLUSIONS

In the current study, the seasonal variability in chl *a* near OSP observed by BGC-Argo in 2012 is reproduced with a 1D physical–biological model, and the model was applied to investigate the mechanisms de-

terminating the variability in phytoplankton biomass, although there may be potential restrictions, as only 1 yr of observations were used to validate the model. Fe plays an important role in regulating the marine ecosystem in the SNEP; thus, the accuracy and completeness of Fe process simulations are necessary and essential. The Fe cycle is incorporated into the model to delineate the HNLC characteristics at OSP. The improvement in the Fe cycle in biogeochemistry models has been an important effort over the past few decades. In this study, the 1D model of Xiu & Chai (2021) was equipped with a cutting-edge Fe cycle added to the original biogeochemistry model (Xiu & Chai 2014, Ma et al. 2019). Different Fe species are included in the Fe cycle, associating with the conversion among them. A large range of Fe species and their complex interconversion processes have the capability to reproduce the processes of the Fe cycle in the ocean, which have not been applied in previous modeling studies of the SNEP.

Furthermore, the loss of microzooplankton during winter is reduced in the model to simulate the overwintering of microzooplankton at OSP. The model can describe the seasonal variability in chl *a* well and reveals that the low phytoplankton biomass in winter is mainly related to weak light conditions and limited Fe concentration. Additionally, the growth of phytoplankton depends on the average light intensity within the MLD rather than surface light. However, unlike the spring phytoplankton bloom observed in the SNWP, the growth of phytoplankton biomass at OSP remains low as light limitation is alleviated from winter to summer because of low Fe availability and grazing pressure from overwintering microzooplankton. Phytoplankton biomass increases in late spring and early summer due to consumption of atmospherically deposited Fe as well as increases in temperature and light. Because of the persistent grazing pressure, accumulation of small phytoplankton biomass takes a long time. In late summer and autumn, chl *a* levels remain high because mesozooplankton grazing reduces the microzooplankton biomass. The application of the model equipped with a comprehensive Fe cycle can help us understand the biogeochemical processes and phytoplankton dynamics in a typical HNLC region, especially the influence of ocean acidification on the change in Fe limitation in the future (Shi et al. 2010).

*Acknowledgements.* We appreciate the data set from World Ocean Atlas (WOA18, <https://www.nodc.noaa.gov/OC5/woa18/>), the float data ([www.mbari.org/chemsensor/floatviz.htm](http://www.mbari.org/chemsensor/floatviz.htm)), the NCEP Reanalysis data set (<https://psl.noaa.gov/data/gridded/data.ncep.reanalysis.html>), the global Fe data set from GEOTRACES (<https://www.bodc.ac.uk/geotraces/>

[data/historical/](http://data/historical/)), and the Copernicus-GlobColour data (<http://marine.copernicus.eu/> and <https://hermes.acri.fr/>). The study was funded by National Natural Science Foundation of China (41730536, 41890805, 42030708).

#### LITERATURE CITED

- ✦ Banse K (1991) Rates of phytoplankton cell division in the field and in iron enrichment experiments. *Limnol Oceanogr* 36:1886–1898
- ✦ Behrenfeld MJ (2010) Abandoning Sverdrup's critical depth hypothesis on phytoplankton blooms. *Ecology* 91: 977–989
- ✦ Behrenfeld MJ, Boss ES (2014) Resurrecting the ecological underpinnings of ocean plankton blooms. *Annu Rev Mar Sci* 6:167–194
- ✦ Bif MB, Hansell DA (2019) Seasonality of dissolved organic carbon in the upper northeast Pacific Ocean. *Global Biogeochem Cycles* 33:526–539
- ✦ Boyd P, Harrison PJ (1999) Phytoplankton dynamics in the NE subarctic Pacific. *Deep Sea Res II* 46:2405–2432
- ✦ Boyd PW, Strom S, Whitney FA, Doherty S, Varela DE (1995) The NE subarctic Pacific in winter: I. Biological standing stocks. *Mar Ecol Prog Ser* 128:11–24
- ✦ Boyd PW, Muggli DL, Varela DE, Goldblatt RH, Goldblatt R, Orians KJ, Orians PJ (1996) *In vitro* iron enrichment experiments in the NE subarctic Pacific. *Mar Ecol Prog Ser* 136:179–193
- ✦ Boyd PW, Berges JA, Harrison PJ (1998) *In vitro* iron enrichment experiments at iron-rich and-poor sites in the NE subarctic Pacific. *J Exp Mar Biol Ecol* 227:133–151
- ✦ Boyd PW, Law CS, Wong CS, Nojiri Y and others (2004) The decline and fate of an iron-induced subarctic phytoplankton bloom. *Nature* 428:549–553
- ✦ Chien CT, Mackey KRM, Dutkiewicz S, Mahowald NM, Prospero JM, Paytan A (2016) Effects of African dust deposition on phytoplankton in the western tropical Atlantic Ocean off Barbados. *Global Biogeochem Cycles* 30: 716–734
- ✦ Cummins PF, Lagerloef GSE (2004) Wind-driven inter-annual variability over the northeast Pacific Ocean. *Deep Sea Res I* 51:2105–2121
- Dagg MJ (1993) Grazing by the copepod community does not control phytoplankton production in the subarctic Pacific Ocean. *Prog Oceanogr* 40:1431–1445
- ✦ de Boyer Montegut C, Madec G, Fischer AS, Lazar A, Iudicone D (2004) Mixed layer depth over the global ocean: an examination of profile data and a profile-based climatology. *J Geophys Res* 109:C12003
- ✦ Denman KL, Peña MA (1999) A coupled 1-D biological/physical model of the northeast subarctic Pacific Ocean with iron limitation. *Deep Sea Res II* 46:2877–2908
- ✦ Denman KL, Peña MA (2002) The response of two coupled one-dimensional mixed layer/planktonic ecosystem models to climate change in the NE subarctic Pacific Ocean. *Deep Sea Res II* 49:5739–5757
- Evans GT, Parslow JS (1985) A model of annual plankton cycles. *Biol Oceanogr* 3:327–347
- ✦ Fennel K, Boss E (2003) Subsurface maxima of phytoplankton and chlorophyll: steady-state solutions from a simple model. *Limnol Oceanogr* 48:1521–1534
- ✦ Findlay HS, Yool A, Nodale M, Pitchford JW (2006) Modeling of autumn plankton bloom dynamics. *J Plankton Res* 28:209–220

- Freeland H (2007) A short history of Ocean Station Papa and Line P. *Prog Oceanogr* 75:120–125
- Frost BW (1987) Grazing control of phytoplankton stock in the open subarctic Pacific Ocean: a model assessing the role of mesozooplankton, particularly the large calanoid copepods. *Mar Ecol Prog Ser* 39:49–68
- Frost BW (1993) A modelling study of processes regulating plankton standing stock and production in the open subarctic Pacific Ocean. *Prog Oceanogr* 32:17–56
- Fujii M, Yoshie N, Yamanaka Y, Chai F (2005) Simulated biogeochemical responses to iron enrichments in three high nutrient, low chlorophyll (HNLC) regions. *Prog Oceanogr* 64:307–324
- Fujii M, Yamanaka Y, Nojiri Y, Kishi MJ, Chai F (2007) Comparison of seasonal characteristics in biogeochemistry among the subarctic North Pacific stations described with a NEMURO-based marine ecosystem model. *Ecol Modell* 202:52–67
- Fujiki T, Matsumoto K, Mino Y, Sasaoka K and others (2014) The seasonal cycle of phytoplankton community structure and photo-physiological state in the western subarctic gyre of the North Pacific. *Limnol Oceanogr* 59: 887–900
- Garcia HE, Weathers K, Paver CR, Smolyar I and others (2018) World Ocean Atlas 2018, Vol 4: dissolved inorganic nutrients (phosphate, nitrate and nitrate+nitrite, silicate). NOAA Atlas NESDIS 84. NOAA National Centers for Environmental Information, Silver Spring, MD
- Geng B, Xiu P, Shu C, Zhang WZ, Chai F, Li S, Wang D (2019) Evaluating the roles of wind and buoyancy flux induced mixing on phytoplankton dynamics in the northern and central South China Sea. *J Geophys Res Oceans* 124:680–702
- Gledhill M, Buck KN (2012) The organic complexation of iron in the marine environment: a review. *Front Microbiol* 3:69
- Goldblatt RH, Mackas DL, Lewis AG (1999) Mesozooplankton community characteristics in the NE subarctic Pacific. *Deep Sea Res II* 46:2619–2644
- Harrison PJ (2002) Station Papa time series: insights into ecosystem dynamics. *J Oceanogr* 58:259–264
- Harrison PJ, Boyd PW, Varela DE, Takeda S, Shiimoto A, Odate T (1999) Comparison of factors controlling phytoplankton productivity in the NE and NW subarctic Pacific gyres. *Prog Oceanogr* 43:205–234
- Harrison PJ, Whitney FA, Tsuda A, Saixop H, Tadokoro K (2004) Nutrient and plankton dynamics in the NE and NW gyres of the subarctic Pacific Ocean. *J Oceanogr* 60: 93–117
- Haskell WZ, Fassbender AJ, Long JS, Plant JN (2020) Annual net community production of particulate and dissolved organic carbon from a decade of biogeochemical profiling float observations in the Northeast Pacific. *Global Biogeochem Cycles* 34:e2020GB006599
- Henson SA, Dunne JP, Sarmiento JL (2009) Decadal variability in North Atlantic phytoplankton blooms. *J Geophys Res Oceans* 114:C04013
- Huston MA, Wolverton S (2009) The global distribution of net primary production: resolving the paradox. *Ecol Monogr* 79:343–377
- Jackson JM, Myers PG, Ianson D (2006) An examination of advection in the northeast Pacific Ocean, 2001–2005. *Geophys Res Lett* 33:L15601
- Jiang M, Barbeau KA, Selph KE, Measures CI, Buck KN, Azam F, Mitchell BG, Meng Z (2013) The role of organic ligands in iron cycling and primary productivity in the Antarctic Peninsula: a modeling study. *Deep Sea Res II* 90: 112–133
- Johnson WK, Miller LA, Sutherland NE, Wong CS (2005) Iron transport by mesoscale Haida eddies in the Gulf of Alaska. *Deep Sea Res II* 52:933–953
- Kalnay E, Kanamitsu M, Kistler R, Collins W and others (1996) The NCEP/NCAR 40-year reanalysis project. *Bull Am Meteorol Soc* 77:437–472
- Kara AB, Rochford PA, Hurlburt HE (2003) Mixed layer depth variability over the global ocean. *J Geophys Res Oceans* 108:3079
- Kawamiya M, Kishi MJ, Yamanaka Y, Suginohara N (1995) An ecological–physical coupled model applied to Station Papa. *J Oceanogr* 51:635–664
- Lam PJ, Bishop JKB, Henning CC, Marcus MA, Waychunas GA, Fung IY (2006) Wintertime phytoplankton bloom in the subarctic Pacific supported by continental margin iron. *Global Biogeochem Cycles* 20:GB1006
- Landry MR, Monger BC, Selph KE (1993) Time-dependency of microzooplankton grazing and phytoplankton growth in the subarctic Pacific. *Prog Oceanogr* 32:205–222
- Landry MR, Barber RT, Bidigare RR, Chai F and others (1997) Iron and grazing constraints on primary production in the central equatorial Pacific: an EqPac synthesis. *Limnol Oceanogr* 42:405–418
- Lee BG, Fisher NS (1993) Release rates of trace elements and protein from decomposing planktonic debris. 1. Phytoplankton debris. *J Mar Res* 51:391–421
- Letelier RM, Karl DM, Abbott MR, Bidigare RR (2004) Light driven seasonal patterns of chlorophyll and nitrate in the lower euphotic zone of the North Pacific Subtropical Gyre. *Limnol Oceanogr* 49:508–519
- Ma W, Xiu P, Chai F, Li H (2019) Seasonal variability of the carbon export in the central South China Sea. *Ocean Dyn* 69:955–966
- Maldonado MT, Boyd PW, Harrison PJ, Price NM (1999) Co-limitation of phytoplankton growth by light and Fe during winter in the NE subarctic Pacific Ocean. *Deep Sea Res II* 46:2475–2485
- Mann KH, Lazier J (1996) Dynamics of marine ecosystems: biological–physical interactions in the oceans, 2<sup>nd</sup> edn. Blackwell Science, Malden, MA
- Marchetti A, Sherry ND, Kiyosawa H, Tsuda A, Harrison PJ (2006) Phytoplankton processes during a mesoscale iron enrichment in the NE subarctic Pacific: part I—biomass and assemblage. *Deep Sea Res II* 53:2095–2113
- Martin JH, Fitzwater SE (1988) Iron deficiency limits phytoplankton growth in the north-east Pacific subarctic. *Nature* 331:341–343
- Martin JH, Gordon RM, Fitzwater S, Brokenow WW (1989) Vertex: phytoplankton/iron studies in the Gulf of Alaska. *Deep Sea Res II* 30:649–680
- Martin JH, Fitzwater SE, Gordon RM (1991) We still say iron deficiency limits phytoplankton growth in the subarctic Pacific. *J Geophys Res* 96:20699–20700
- Matsumoto K, Honda MC, Sasaoka K, Wakita M, Kawakami H, Watanabe S (2014) Seasonal variability of primary production and phytoplankton biomass in the western Pacific subarctic gyre: control by light availability within the mixed layer. *J Geophys Res Oceans* 119:6523–6534
- Miller CB, Clemons MJ (1988) Revised life history analysis for large grazing copepods in the subarctic Pacific Ocean. *Prog Oceanogr* 20:293–313
- Miller CB, Frost BW, Wheeler PA, Landry MR, Welschmeyer

- N, Powell TM (1991) Ecological dynamics in the subarctic Pacific, a possibly iron-limited ecosystem. *Limnol Oceanogr* 36:1600–1615
- ✦ Mochizuki M, Shiga N, Saito M, Imai K, Nojiri Y (2002) Seasonal changes in nutrients, chlorophyll *a* and the phytoplankton assemblage of the western subarctic gyre in the Pacific Ocean. *Deep Sea Res II* 49:5421–5439
- ✦ Nishioka J, Obata H, Ogawa H, Ono K, Yasuda I (2020) Subpolar marginal seas fuel the North Pacific through the intermediate water at the termination of the global ocean circulation. *Proc Natl Acad Sci USA* 117:12665–12673
- ✦ Obayashi Y, Tanoue E, Suzuki K, Handa N, Nojiri Y, Wong CS (2001) Spatial and temporal variabilities of phytoplankton community structure in the northern North Pacific as determined by phytoplankton pigments. *Deep Sea Res I* 48:439–469
- Parsons TR, Lalli CM (1988) Comparative oceanic ecology of the plankton communities of the subarctic Atlantic and Pacific Oceans. *Oceanogr Mar Biol Annu Rev* 26:317–359
- ✦ Peña MA (2003) Modelling the response of the planktonic food web to iron fertilization and warming in the NE subarctic Pacific. *Prog Oceanogr* 57:453–479
- ✦ Peña MA, Varela DE (2007) Seasonal and interannual variability in phytoplankton and nutrient dynamics along Line P in the NE subarctic Pacific. *Prog Oceanogr* 75:200–222
- ✦ Plant JN, Johnson KS, Sakamoto CM, Jannasch HW, Coletti LJ, Riser SC, Swift DD (2016) Net community production at Ocean Station Papa observed with nitrate and oxygen sensors on profiling floats. *Global Biogeochem Cycles* 30: 859–879
- ✦ Rijkenberg M, Fischer AC, Kroon JJ, Gerringa L, Timmermans KR, Wolterbeek HTh, de Baar HJW (2005) The influence of UV irradiation on the photoreduction of iron in the Southern Ocean. *Mar Chem* 93:119–129
- ✦ Sasai Y, Yoshikawa C, Smith SL, Hashioka T and others (2016) Coupled 1-D physical–biological model study of phytoplankton production at two contrasting time-series stations in the western North Pacific. *J Oceanogr* 72: 509–526
- ✦ Schallenberg C, Davidson AB, Simpson KG, Miller LA, Cullen JT (2015) Iron(II) variability in the northeast subarctic Pacific Ocean. *Mar Chem* 177:33–44
- ✦ Schallenberg C, Ross ARS, Davidson AB, Stewart GM, Cullen JT (2017) Temporal variability of dissolved iron species in the mesopelagic zone at Ocean Station PAPA. *J Mar Syst* 172:128–136
- ✦ Shi DL, Xu Y, Hopkinson BM, Morel F (2010) Effect of ocean acidification on iron availability to marine phytoplankton. *Science* 327:676–679
- Sigman DM, Hain MP (2012) The biological productivity of the ocean. *Nature Educ Knowl* 3:1–16
- ✦ Simon N, Cras AL, Foulon E, Lemée R (2009) Diversity and evolution of marine phytoplankton. *C R Biol* 332:159–170
- ✦ Strom SL, Miller CB, Frost BW (2000) What sets lower limits to phytoplankton stocks in high-nitrate, low-chlorophyll regions of the open ocean? *Mar Ecol Prog Ser* 193:19–31
- ✦ Sunda WG, Huntsman SA (1997) Interrelated influence of iron, light and cell size on marine phytoplankton growth. *Nature* 390:389–392
- ✦ Sverdrup HU (1953) On conditions for the vernal blooming of phytoplankton. *J Cons Cons Int Explor Mer* 18:287–295
- ✦ Tagliabue A, Mtshali T, Aumont O, Bowie AR, Klunder MB, Roychoudhury AN, Swart S (2012) A global compilation of dissolved iron measurements: focus on distributions and processes in the Southern Ocean. *Biogeosciences* 9: 2333–2349
- ✦ Taylor JR, Ferrari R (2011) Shutdown of turbulent convection as a new criterion for the onset of spring phytoplankton blooms. *Limnol Oceanogr* 56:2293–2307
- ✦ Timothy DA, Wong CS, Barwell-Clarke JE, Page JS, White LA, Macdonald RW (2013) Climatology of sediment flux and composition in the subarctic Northeast Pacific Ocean with biogeochemical implications. *Prog Oceanogr* 116: 95–129
- ✦ Westberry TK, Schultz P, Behrenfeld MJ, Dunne JP and others (2016) Annual cycles of phytoplankton biomass in the subarctic Atlantic and Pacific Ocean. *Global Biogeochem Cycles* 30:175–190
- ✦ Whitney FA, Wong CS, Boyd PW (1998) Interannual variability in nitrate supply to surface waters of the Northeast Pacific Ocean. *Mar Ecol Prog Ser* 170:15–23
- ✦ Wong CS, Matear RJ (1999) Silicate limitation of phytoplankton productivity in the northeast subarctic Pacific. *Deep Sea Res 2 Top Stud Oceanogr* 46:2539–2555
- ✦ Xiu P, Chai F (2014) Connections between physical, optical and biogeochemical processes in the Pacific Ocean. *Prog Oceanogr* 122:30–53
- ✦ Xiu P, Chai F (2021) Impact of atmospheric deposition on carbon export to the deep ocean in the subtropical Northwest Pacific. *Geophys Res Lett* 48:e2020GL089640
- ✦ Yang B, Emerson SR, Peña MA (2018) The effect of the 2013–2016 high temperature anomaly in the subarctic Northeast Pacific (the 'Blob') on net community production. *Biogeosciences* 15:6747–6759

*Editorial responsibility: Alejandro Gallego,  
Aberdeen, UK  
Reviewed by: R. Maria Letelier and 2 anonymous referees*

*Submitted: January 10, 2021  
Accepted: September 23, 2021  
Proofs received from author(s): November 5, 2021*